Computational Materials Science 103 (2015) 68–76

Contents lists available at ScienceDirect

Computational Materials Science

journal homepage: www.elsevier.com/locate/commatsci

Thermal resistance from irradiation defects in graphite

Laura de Sousa Oliveira, P. Alex Greaney *

School of Mechanical, Industrial & Manufacturing Engineering, Oregon State University, Corvallis, OR 97331, United States

ARTICLE INFO

Article history:
Received 25 November 2014
Received in revised form 23 February 2015
Accepted 3 March 2015
Available online 2 April 2015

Keywords:
Thermal conductivity
Graphite
Point defects
Molecular dynamics
Irradiation defects
Heat conduction

ABSTRACT

An atomistic level understanding of how varying types and numbers of irradiation induced defects affect thermal resistance in graphite is vital in designing accident tolerant fuels for next-generation nuclear reactors. To this end we performed equilibrium molecular dynamics simulations and computed the change to thermal conductivity due to a series of clustering and non-clustering point defects using the Green–Kubo method. In addition, we present a comprehensive discussion of several approaches to converge the integral of the heat current autocorrelation function. Our calculations show that more energetically favorable clustering defects exhibit fewer low frequency modes and increase the anisotropic nature of graphite selectively exerting a significant effect on thermal resistance along the *c*-axis.

1. Introduction

In the early 1940s, polycrystalline graphite was the only abundantly produced material with the required purity to be used as a moderator in nuclear reactors [1]. While other reactor materials have since been adopted, at the present time, graphite is still in high demand for the development of high-tech fuel elements for next-generation nuclear reactors. Graphite or pyrolytic carbon is included in nuclear fuel assemblies to encapsulate the fissile material. In these applications, in addition to utilizing its high temperature strength, the graphite acts as a neutron moderator and reflector. In some fuels graphite encapsulates the fissile materials in which case all the heat produced by fission in a fuel pin must be conducted out through the graphite. As the moderating properties of graphite are temperature dependent, accurately predicting the thermal conductivity of graphite and other fuel assembly materials—including how their thermal conductivity evolves under irradiation—is vitally important for the design of accident tolerant fuels.

The thermal conductivity (κ) of graphite is experimentally found to change with synthesis conditions and while in service as a direct result of radiation [2]. This indicates that κ is not an intrinsic property and is instead governed by the defect morphology of the graphite. Simulations typically measure intrinsic properties, but we aim to determine an atomistic level understanding of scattering processes from collections of irradiation induced point defects and to establish a systematic understanding of how defect type, number and different defect-type ensembles affect thermal resistance and phonon mean free path in graphite. We do so with the goal that the insight that we gain can be incorporated into approaches for quantitatively predicting the lattice thermal conductivity that are based on solving the Boltzmann transport equation. Such a tool would be useful to nuclear engineers and materials scientists in the process of designing new reactors and fuel systems that are accident tolerant. As the first step along this path, we have computed the energy and structure of a zoo of point defects and determined their separate effects on thermal conductivity along and across the basal plane.

In Section 2 we establish and validate our method for computing thermal conductivity of defect-free graphite. More specifically, we discuss advantages and challenges associated with the Green–Kubo formalism: in Section 2.1 we discuss different approaches to converge the heat current autocorrelation function (HCACF) and propose a solution based on our findings; the issue of size convergence is explained and addressed in Section 2.2. After establishing an adequate system size, we introduce defects and compute their formation energies in Section 3. Values are obtained using classical molecular dynamics and compared with density functional theory (DFT) calculations. Interstitial defects are also annealed to find the most energetically favorable configuration. In Section 4 we compare the perfect crystalline system, where transport is limited by crystal lattice anharmonicity and the acoustic phonons carrying the bulk of heat are only scattered by other phonons, with systems with point defects, where defect scattering is expected to play a

* Corresponding author. Tel.: +1 541 737 3048.
E-mail address: alex.greaney@oregonstate.edu (P.A. Greaney).
URL: http://research.engr.oregonstate.edu/greaney/ (P.A. Greaney).

http://dx.doi.org/10.1016/j.commatsci.2015.03.001
0927-0256/

crucial role in thermal transport. Concluding remarks are presented in Section 5.

2. Computational method and validation

Molecular dynamics modeling captures the anharmonic interactions of atomic vibrations that carry heat and both equilibrium and non-equilibrium simulations can be used to predict thermal conductivity [3]. The Green–Kubo formalism [4,5] is a well established equilibrium molecular dynamics approach that has been used successfully to compute thermal conductivity in a wide range of materials from silicon [6] to metal–organic-frameworks [7]. This method is derived from the fluctuation–dissipation theorem and computes the thermal conductivity, κ, from the equilibrium fluctuations in the heat current vector, $\mathbf{J}$, by:

$$\kappa_{xx} = \frac{V}{k_B T^2} \int_0^\infty C_{\mathbf{J}xx}(\tau)\, d\tau, \tag{1}$$

where k_B, T and V are the Boltzmann's constant, temperature and volume of the simulated region respectively. The term $C_{\mathbf{J}}(\tau) = \langle \mathbf{J}(t)\mathbf{J}(t+\tau)\rangle$, and is the non-normalized heat current autocorrelation function (HCACF). The net flow of heat fluctuates about zero at equilibrium and the thermal conductivity is related to how long it takes for the fluctuations to dissipate. Both equilibrium and non-equilibrium molecular dynamics (NEMD) simulations suffer from size artifacts that must be mitigated. In NEMD, the simulated system size must be larger than the intrinsic mean-free path of the phonons in order to eliminate ballistic transport between the heat source and sink [3]. Equilibrium MD affords one a smaller system size as phonons may move through periodic boundaries unhindered.

Simulations were performed with the large-scale equilibrium classical molecular dynamics software LAMMPS [8]. After relaxing the atomic structure, along with the size of the compute cell, all systems were given a thermal energy equivalent to 300 K and equilibrated in the microcanonical ensemble (NVE) for 50 ps before starting to record the HCACF. The simulations were then performed for an additional 0.6 ns with a 0.2 fs time step and periodic boundary conditions. Throughout the period in NVE the average temperature remained at approximately 300 K. This is well below the Debye temperature for graphite (approximately 2500 K in the basal plane and 950 K along the *c*-axis [2]). However, our goal is a comparative analysis of phonon scattering from and around the defect. As scattering from classically occupied high frequency modes is present with and without the defect this has little contribution to the *change* in κ. The adaptive intermolecular reactive empirical bond-order (AIREBO) potential function formulated by Stuart et al. [9] was used for all simulations. The AIREBO potential includes anharmonic terms in the carbon bonds, an adaptive treatment of the non-bonded and dihedral angle interactions and has the capability to model the interaction between layers in graphite [9]. Two main challenges result from using the Green–Kubo: (1) determining an appropriate system size and (2) converging the HCACF. We shall first address the latter challenge and propose a solution based on the work of Chen et al. [10].

2.1. HCACF convergence

There is no average heat flux, $\langle \mathbf{J}\rangle$, for a system in equilibrium, and the HCACF, *i.e.* the term inside the integral in Eq. (1), is therefore expected to decay to zero given sufficient time. Instead, long lived oscillations with a significant contribution to the computed thermal conductivity have been observed [11–14]; this behavior is illustrated in Fig. 1. The HCACF is crucial in computing κ using the Green–Kubo method and yet there is little consensus among researchers on whether these oscillations are significant to thermal transport or a result of noise, and as to what approach to take. A discussion of this behavior and of possible approaches to converging the HCACF is essential in understanding the limitations of the Green–Kubo formalism and validating thermal transport calculations.

Fig. 1(a) shows the accumulation of the averaged HCACF along a basal direction over a typical simulation. It can be seen that the tail of the HCACF contains many fluctuations, but rather than these decaying smoothly as more data is averaged there occur sporadic events that can overwhelm the average to add new fluctuations to $C_J(\tau)$ and significantly change the initial value $C_J(0)$. These large events show up in the majority of simulations and for all simulated system sizes. Long lasting oscillations are prevalent along the basal plane and are different from oscillations along the *c*-axis (see Fig. 1). Fluctuations along the *c*-axis exhibit a higher frequency and oscillate around zero with the HCACF converging to zero with only minor instabilities affecting its integral. Fluctuations along the basal plane, on the other hand, do not fade away during computation time and significantly affect κ. In graphite, κ calculations in the *c*-direction are not affected by HCACF fluctuations as much as basal plane calculations are. This makes results perpendicular to the basal plane easier to compute and more reliable.

Along the basal plane the HCACF exhibits a two-stage decay: a rapid decay associated with high frequency phonons and a slower decay associated with lower frequency phonons. Similar two-stage decay (or three-stage decay) is observed in many single element materials and different authors have modeled κ by fitting the HCACF to the sum of two or more exponentials [13–15]. This is a more physically meaningful approach than a single exponential fit in that it captures multiple relaxation processes, but it neglects the contribution of the HCACF tail, which results in a systematic underestimation of κ [3,14]. When addressing the issue of convergence in the HCACF we have examined a wide variety of strategies. These strategies include direct integration of the HCACF truncated to various cutoffs, fits of varying sums of exponentials to the truncated HCACF, and fits in the frequency domain. Here we present only a few of the best or otherwise insightful findings and a brief discussion of our approach.

(i–iv) Direct numerical integration of the truncated HCACF up to (i) 50 ps along *z* and 20 ps along *x* and *y*, (ii) 5 ps, and (iii–iv) a noise dependent cut off time, t_c, proposed by Chen et al. and described below [10]. For (iv) individual cut-offs were computed for each HCACF as shown in Fig. 1(b)–(d), and for (iii) an average t_c was used for each simulation set.

(v) Single exponential fits to the first 5 ps of the HCACF.

(vi) The fitting procedure proposed by Chen et al., which includes a fixed offset term in the fitting function:

$$\frac{C_{\mathbf{J}}(\tau)}{C_{\mathbf{J}}(0)} = A_1 e^{-\tau/t_1} + A_2 e^{-\tau/t_2} + Y_0, \tag{2}$$

such that κ is computed as

$$\kappa_{xx} = \frac{V C_{\mathbf{J}xx}(0)}{k_B T^2}(A_1 t_1 + A_2 t_2 + Y_0 t_c), \tag{3}$$

where A_1, A_2, Y_0, t_1 and t_2 are fitting parameters. Chen et al. argue that including the offset Y_0 reduces the computational error. In our implementation of this we used the simplex method to optimize the fit variables. It is physically meaningless to have negative Y_0 and this term was weighed with a Heaviside function to prohibit negative Y_0 terms. We also imposed the condition that $A_1 + A_2 + Y_0 = 1$.

(vii) Double exponential of the form in (vi) with Y_o set to zero.

(viii) Triple exponential of the form:

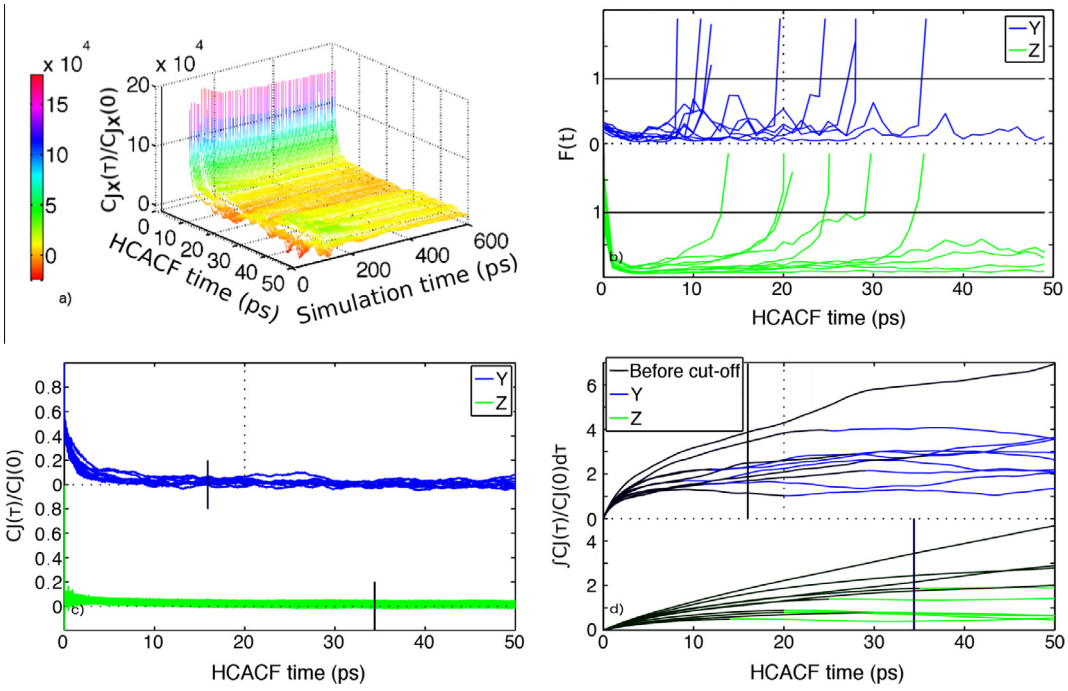

Fig. 1. In (a), the HCACF is computed as the simulation progresses along x for the perfectly crystalline $11 \times 11 \times 11$ supercell. At first only a few values contribute to the ensemble average and the initial HCACFs are noisy. As the averaging time progresses the HCACF becomes smoother with the exception of well defined crests and troughs, most of which do not fade away during the total simulation time. (b), (c) and (d) correspond to the HCACF noise (computed as $F(t)$), the final HCACF, and the integral of the HCACF, respectively, for all simulations of the perfect $11 \times 11 \times 11$ supercell system along y and z (or c). In (d), the black curves correspond to each individual simulation before its cut-off time, and in (c) and (d) the vertical black lines indicate the average cut-off time of all simulations, as described in the text.

$$\frac{C_J(\tau)}{C_J(0)} = A_1 e^{-\tau/t_1} + A_2 e^{-\tau/t_2} + (1 - A_1 - A_2) e^{-\tau/t_3}, \tag{4}$$

fit to each HCACF.

The issue of the cut-off time should now be discussed, before analyzing the results in Fig. 2. The necessity to truncate the HCACF is illustrated in Fig. 1 in which it can be seen that after roughly 2–5 ps the integrals of the autocorrelations diverge even though the HCACF is almost zero. This divergence arises from the integration of random fluctuations in $C_J(\tau)$ effectively adding a random walk to the integral of $C_J(\tau)$. The error from this random walk grows over time, while the systematic error from omitting the long tail of slow decay processes in the HCACF diminishes over time. There exists an optimal truncation point that minimizes the error in the integral of $C_J(\tau)$, but there is little consensus in the literature on how to determine it [12,3]. While selecting a consistent cut-off may often suffice to obtain a comparative analysis, it introduces a systematic error in the estimation of the HCACF, potentially neglecting the contribution of lower phonon modes to k. Chen et al. [10] propose obtaining a quantitative description of the numerical noise in the relative fluctuation of the HCACF, F(t), defined as

$$F(t) = \left| \frac{\sigma(C_J)}{E(C_J)} \right|, \tag{5}$$

where σ is the standard deviation and E the expected value of the HCACF in an interval $(t, t + \delta t)$. The cut-off point is determined to be above an $F(t)$ of 1 (see Fig. 1(b)–(d)), *i.e.* when the scale of the fluctuations become the same as the mean. Chen et al. suggest that $F(t)$ is insensitive to the choice of δ. We find this is the case for only small variations and between a δ of 1, 3, and 5 ps the best results correspond to the 1 ps interval. Both 3 and 5 ps intervals resulted in outliers with a significant effect on κ. The variability we observed with the choice of δ suggests that obtaining a good fit using this method requires a balance between having sufficient data points to compute the local averages while maintaining enough temporal resolution to reasonably determine at what time the noise exceeds $F(t) = 1$. A cut-off point was computed for each run and the average cut-off point for a given system was then obtained. Curves without a cut-off up to the maximum HCACF time computed for each direction were factored in with a cut-off equivalent to the total HCACF time. Each system was simulated 10 times. We compared κ for the cases when δ was 1, 3 and 5 ps with κ being computed using both each independent simulation's cut-off (as in Chen et al.) and using the average cut-off for all simulations. We found that using the average cut-off yielded similar results with error bars significantly smaller than using the corresponding systems' individual run cut-offs to compute κ for each simulation within a cell size. In theory, if we could consider the average local fluctuations in the heat flux over an infinite amount of time, we should be able to find a "true" thermal conductivity of a given system. It is then reasonable to assume that each HCACF is an approximation to an HCACF obtained over infinite time and that there is a "true" cut-off point, thus providing an argument for using the average cut-off on each individual run to compute κ.

When only the first two terms of the HCACF were computed, as in (vii), Y_0 contributed up to over 100 W/(mK) in the most extreme case. This illustrates the insufficiency of the two exponential fits to estimate κ. The sum of three exponential fits yields results very similar to the strategy adopted by Chen et al. with the added modification of using the average cut-off instead of each individual simulation's cut-off. However, as the number of fitting variables increases, results are expected to mimic those of a full integration and the fit loses its physical significance. This correspondence nevertheless suggests Eq. (4) to be an adequate fit and substantiates the cut-off method. More strikingly, simply using the average cut-off as the HCACF integration limit yields similar results

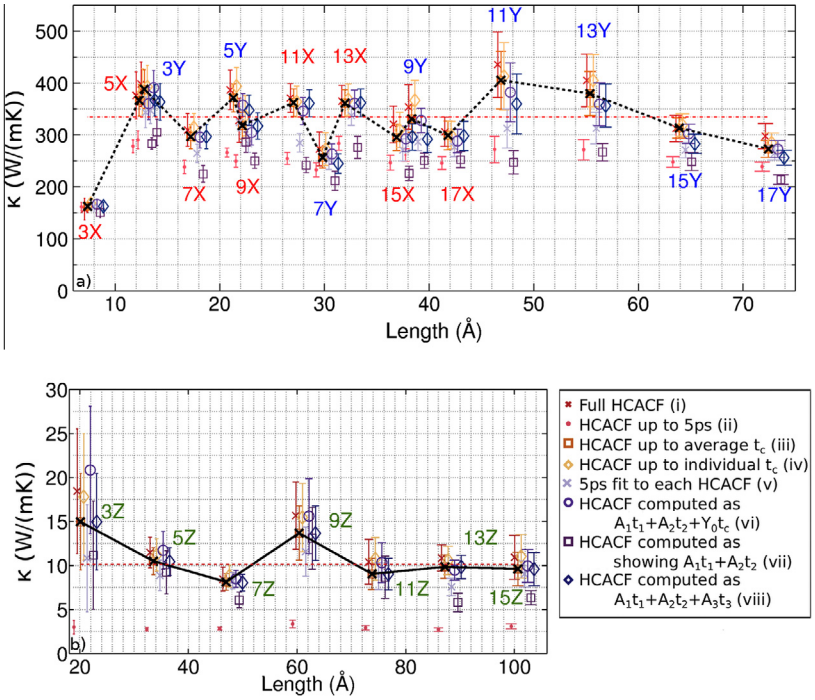

Fig. 2. (a) corresponds to κ measured for different supercells along x and y in the basal plane and (b) to κ computed along the c-axis. The text in (a) corresponds to the direction in which κ was measured (x or y) and the supercell size along that direction. The x-axis in (a) and (b) corresponds to the actual supercell length along the specified direction—note that the cluster of points for a single length have been spaced out slightly in x in order to make the plot more readable by removing overlays of error bars. The black crosses mark the true abscissa of all error bars in a cluster of points, labeled (i) to (viii). In addition to establishing size convergence, the figures illustrate a set of different approaches (labeled in the legend) considered to converge the HCACF and the corresponding standard error. Method (iii) was selected; in (a) the error bars corresponding to this method have been made to coincide with the true length (marked with Xs), around which the other error bars are distributed.

with error bars comparable to the fit. The correct behavior of the HCACF along the basal plane is thus more accurately explained by the fit type suggested by Chen et al. than merely the sum of exponentials, but in order to compute actual κ values, the fit introduces an unnecessary hassle to no gain. Furthermore, the nature of the HCACF along the c-axis is very different than that of the basal plane, as can be seen by looking at Figs. 1 and 2, and this fit type is not adequate to explain the HCACF perpendicular to the basal plane. That said, the error bars are noticeably smaller when the HCACF is integrated only up to t_c than when they are integrated over the total HCACF time. Note that the HCACF is computed up to 20 ps along the basal plane and 50 ps along the c-axis. This is because along the c-axis the tail of the HCACF has an increased contribution to the total thermal conductivity. The same does not occur along the basal plane, as evidenced by a comparison between the fit (vi), suggested by Chen et al., and (iii), the method selected. We have furthermore observed no trend in the truncation time with size. Instead, a systematic error appears to be introduced for a given system size where κ values in both x and y tend to be either above or below the mean thermal conductivity of all systems' simulations. The simplest, most effective approach is to select the cut-off for each simulation by setting $F(t) = 1$ and to use the average cut-off of all simulations when computing each simulation's individual κ. This method is adequate to compute κ along any direction for highly oriented graphite.

While there is no consensus on the best method to reduce noise and capture the nature of the HCACF of graphite and other materials, the approach selected in this paper yields κ estimates higher than a sum of exponentials, with moderately small error bars and without the need of a complicated fit. This method was used for all defect calculations along the basal plane and along c, taking into account that the cut-off along c must neglect the first values of $F(t) \geq 1$ that take place in the initial decay stages (see Fig. 1). Being consistent with the choice of method is often sufficient for a significant comparative analysis and this method allows us to do that.

2.2. Size convergence

Periodic boundary conditions allow simulations of a small number of particles to mimic the behavior of an infinite solid; however, they limit the number and wavelength of the vibrational modes available to carry heat. Thus, when using the Green–Kubo method it is first necessary to establish size convergence. Thermal conductivity values were computed for perfectly crystalline systems of varying size, as can be observed in Fig. 2. An 8 atom unit cell was defined and 7 systems ranging between $3 \times 3 \times 3$ and $15 \times 15 \times 15$ supercells and an additional $17 \times 17 \times 11$ supercell system were simulated (again 10 times each). Along the basal plane the systems' size was asymmetric in the x and y dimensions with x smaller than y—this was done to better gauge potential size artifacts. While there was a large variability in the thermal conductivity—the values are scattered between 300 and 400 W/(mK) along the x-direction and 250 and 400 W/(mK) along the y—the system size appears to be converged early on. There is no evidence of a system size artifact, but to be cautious different x and y values were maintained when computing thermal conductivity in defective systems as well. For computations performed with defects, the $11 \times 11 \times 11$ supercell was selected to allow for a big enough compute cell with a feasible computational expense associated. The $11 \times 11 \times 11$ supercell corresponds to a 10648 atom system in the perfect graphite, with a $27.05 \times 46.86 \times 73.79$ Å^3 volume in the x, y, and z directions, respectively.

It is important to note that although the thermal conductivity that we obtain using the Green–Kubo method in the c-direction is close to the experimental value, in the basal direction κ obtained

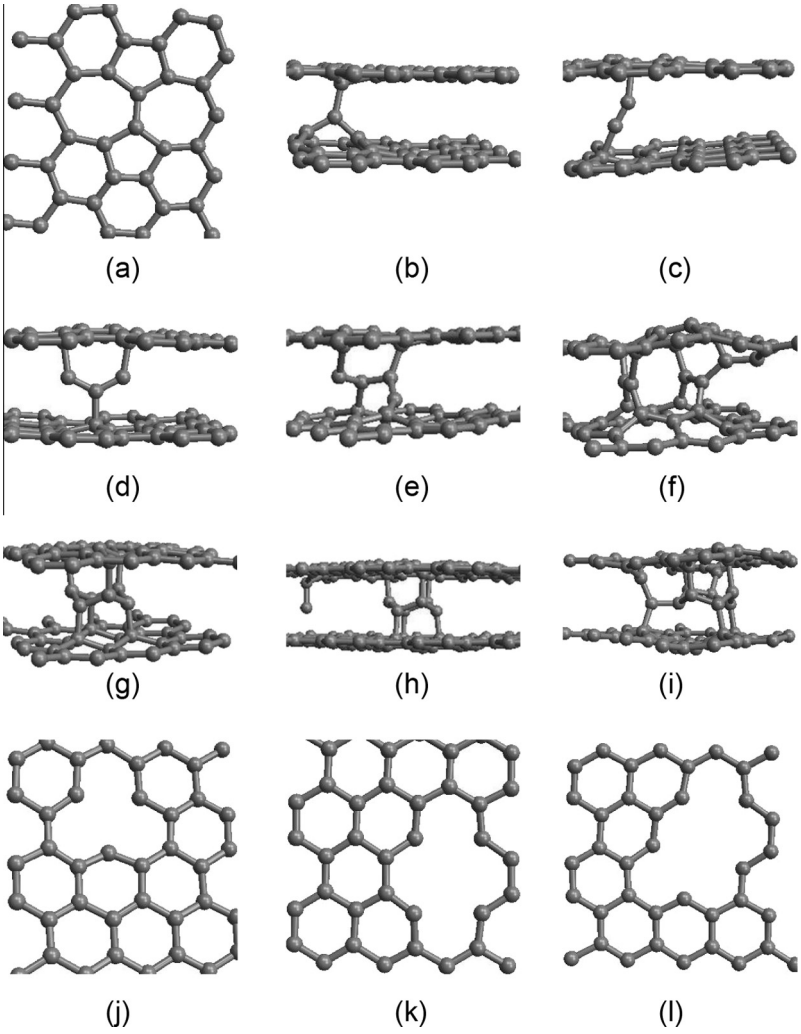

Fig. 3. Illustration of the defects examined in this study: Stone–Wales defect (a); single interstitial (b); 2–8 interstitials (c)–(i); single vacancy (j), di-vacancy (k), and 3 vacancies (l). The interstitial defects are shown in their annealed configurations.

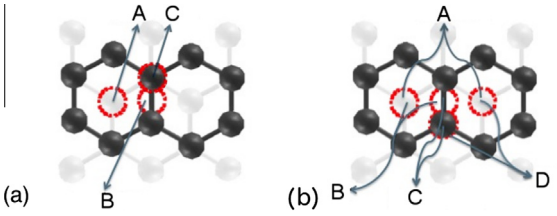

Fig. 4. Possible defect types for single (a) and two-interstitial defects (b).

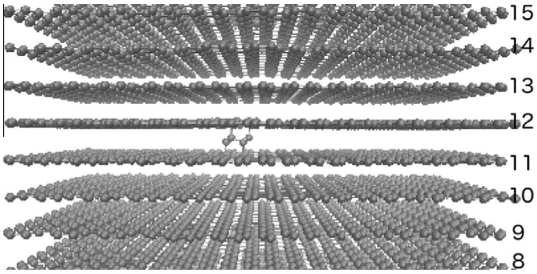

Fig. 5. Slice of a graphite system with an hexagonal platelet, indicating the location of the defect. There are 22 total layers in the system.

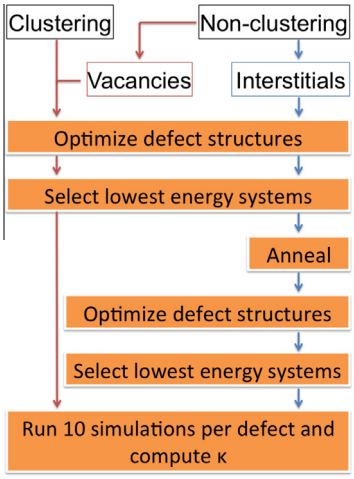

Fig. 6. Schematic of the optimization procedure applied to classically simulated defects before computing formation energies.

from simulations is roughly one order of magnitude lower than the experimentally measured value of 4180 W/(mK) [16]. There are a number of potential sources for this discrepancy that include the classical occupation of high frequency modes, the exclusion of long

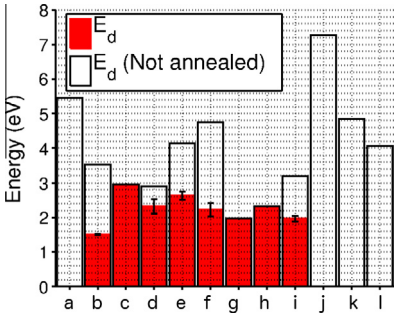

Fig. 7. These energies correspond to the defects depicted in Fig. 3. In the case of the interstitial defect-types, values were computed both for annealed and non-annealed systems.

wavelength modes by the small system size, or incorrect anharmonicity in the interatomic potentials. Without a satisfactory explanation of this discrepancy we proceed (cautiously) and focus on the trend in κ due to defects, and in particular the effect of defects on the c-axis conductivity. To benchmark what might be expected from the introduction of defects, we remark that experimental results have shown a decrease by an approximate factor of 10 for IG-110U and ETP-10 graphite types irradiated at 0.02 dpa (displacements per atom) at 200 °C, with an unirradiated κ of near 100 W/(mK) [17]. The GC-30 type graphite shows only an approximate factor of 4 decrease from unirradiated to irradiated under the same conditions as the aforementioned types, from an initial κ of 16 W/(mK) [17]. All three graphites decreased by an additional factor of 4 when irradiated at 0.25 dpa [17]. Ishiama et al. observe a similar factor of 4 decrease in graphite with an unirradiated value of 160 W/(mK) when exposed to 11.9 dpa radiation at room temperature [18]; such high dpa values would however quickly result in the amorphization of graphite [19] and its anisotropy would be lost.

3. Identifying defect structures

In irradiated graphite carbon atoms are displaced due to cascade reactions giving rise to many point defects in what is termed the Wigner effect. We categorize these into defects that have a strong driving force for clustering, such as vacancies and interstitials, and defects that are less driven to cluster such as bond rotation defects, and isotopic defects. The following clustering defects were considered: a single interstitial (Fig. 3(b)), a single vacancy (Fig. 3(j)), clusters of 2–8 interstitials (Fig. 3(c)–(i)) and clusters of 2–3 vacancies (Fig. 3(k) and (l)). For a single interstitial, three interstitial locations were considered, as depicted in Fig. 4(a). Similarly, four configurations were simulated for 2-interstitial clusters, as shown in Fig. 4(b). The single vacancy site is between the centers of hexagonal voids on the planes adjacent to the plane of the vacancy, *i.e.* where the type A single interstitial is positioned in Fig. 4(a), but in the lower, less visible layer. The added vacancies lie directly between atom sites on the adjacent layers. The non-clustering defects considered were a Stone–Wales defect (Fig. 3(a)) and an isotope. The C^{14} isotope was selected for having a higher mass than C^{13}, another common carbon isotope, and thus being expected to have a higher contribution to changes in κ. The defects were introduced to the center of the selected $11 \times 11 \times 11$ perfect system; the interstitial defects were placed between the 11th and 12th layer of the 22 layer cell, and the remaining defects within the 11th layer, as shown in Fig. 5.

Formation energies were computed using classical MD for all defects. These calculations were used to estimate the likelihood of formation of each defect, where the energy per defect is given by

$$E_d = E_D - \frac{E_O}{N_O} N_D. \tag{6}$$

N_D and N_O are the number of atoms in the defective system and the corresponding non-defective system, in that order. E_D corresponds to the total energy of the system and E_O to the total energy of the perfect system of the same size.

The optimization process for the classical calculations is described in the flowchart in Fig. 6 and was performed using the FIRE scheme [20] as implemented in LAMMPS, thus allowing for both the relaxation of the atomic positions and the supercell size. As part of the process to optimize the geometry of the interstitial defects, platelet-like defects were also annealed and subsequently cooled. The defects were annealed to 1500 K for 500 ps and cooled to 300 K for 1 ns, in the canonical ensemble (NVT). By doing this we allowed the already low energy interstitial defects to migrate and rearrange themselves into potentially lower energy configurations.

Energy values for the different defect types and numbers are depicted in Fig. 7 and in Table 1. Classical interstitial defect energies were computed for the optimized structures before and after annealing. It is notable in Fig. 7, that the annealing process often yielded defect structures with considerably lower energy than those reached by direct relaxation using the FIRE algorithm—even for very simple defects such as a lone interstitial. There is a good agreement between the overall trend of defect energies as modeled with the AIREBO empirical potential and those from Li et al. [21] computed using density functional theory (DFT) with the local density approximation (LDA) (see Table 1). Interestingly, the type *A* single interstitial when annealed becomes structurally similar to Li et al.'s 5.5 eV formation energy "free" interstitial, computed with DFT. Telling et al. find the same low energy configuration value with LDA for a so-called 'spiro-interstitial' (type B in Fig. 4(a)) when the surrounding lattice is sheared approximately half of a bond length towards ABC stacking [22]. Pre-AIREBO MD simulations using an optimized Tersoff potential yielded a 5.8 eV formation energy for a single interstitial [23]. Stone–Wales defects have the lowest formation energy of all intrinsic defects in graphenic systems [24], calculated with DFT at 5.2 eV [21]. A single vacancy of the type simulated in this paper has been computed at 8.2 eV using LDA, and an in-plane divacancy at 8.7 eV (comparable with our 9.7 eV calculation) [22]. In an earlier work, Kaxiras and Pandey reported a 7.6 eV formation energy for a single vacancy [25].

4. Thermal resistance from defects

The computed κ values for nine graphite systems each including a different defect are given in Fig. 8. These systems include the more energetically favorable interstitial platelets, and all values were

Table 1
Classical MD energy calculations for single and double interstitial defect types based on location. The values obtained for a single interstitial are compared with available density functional theory (DFT) calculations using the local density approximation (LDA) from Ref. [21].

Defect type	Single: A	Single: B	Single: C	Two: A	Two: B	Two: C	Two: D
LAMMPS	3.57 eV	4.73 eV	4.46 eV	4.99 eV	3.27 eV	2.95 eV	2.98 eV
Literature (DFT, LDA) [21]	6.7 eV	7.7 eV	7.4 eV	–	–	–	–

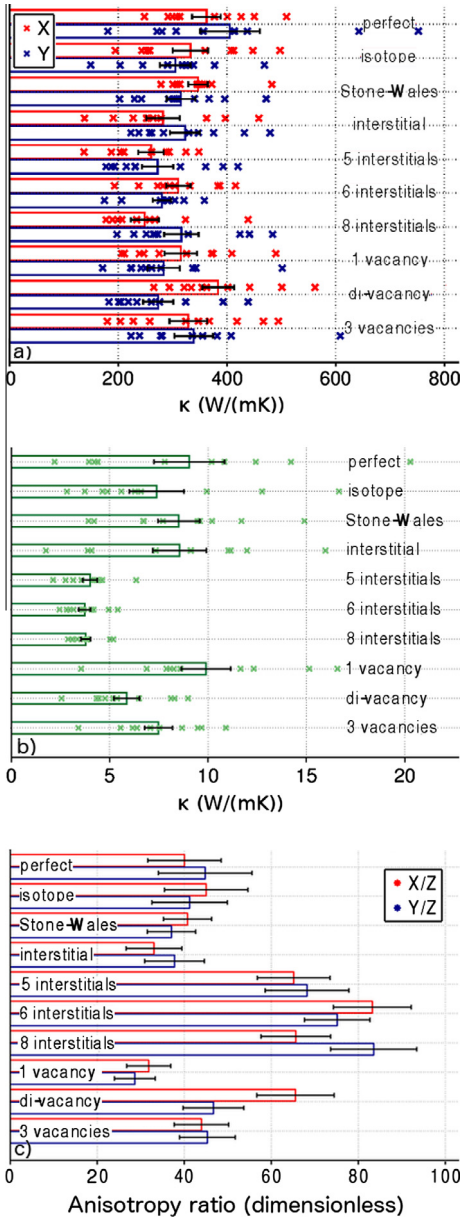

Fig. 8. κ obtained for different defect types along x and y (a) and in the basal plane (b); and the anisotropy ratio, *i.e.* κ_a/κ_c, computed for both x and y for the same defect types (c).

obtained using the Green–Kubo method as with the perfect crystal. For κ in the basal direction, it can be seen that all defects with the exception of vacancies produce a small but pronounced degradation of κ that is outside the error bars of the calculation. Among the defects that reduce κ in the basal direction there is little difference in their impact, with the larger platelet defects providing a fractionally larger reduction in κ. In contrast, the effect on κ in the c-direction is dramatic, with little impact on κ from single atom defects but a large impact from clustered defects, especially clustered interstitials. Interstitial clusters are low energy defects and are therefore more likely to occur under irradiation.

Performing a discrete cosine transform (DCT) of the HCACF reveals the presence of localized modes exclusively associated with the lower thermal conductivity defect types (see Fig. 9). We performed DCTs for the defect systems both along x, y and z, and found two notable differences between systems in the DCT of the c-axis HCACF. Systems containing interstitial platelets developed a series of peaks at $\sim 1.3, 2.5$ and 3 THz. We attribute these to rattling of the platelets in the c-direction and the defects being large enough to have relatively low frequency vibrational modes. More interestingly, there is a dramatic reduction in the intensity of low frequency modes in the HCACF of the systems with diminished thermal conductivity.

Thermal conductivities were also computed for differently sized systems containing the 6 atom (hexagonal) platelet. In the results in Fig. 8 there is little difference in terms of how the number of interstitials in a cluster (between 5 and 8) affect the overall thermal conductivity in the system; however, we expect a dependence on the concentration of defects. To examine this dependence on defect spacing, κ was computed for a number of differently sized systems each containing a hexagonal interstitial platelet (Fig. 10). Additionally, we simulated an $11 \times 11 \times 11$ supercell containing two vertically aligned interstitial platelets thereby altering the c-spacing independent from the basal spacing (the last datum in Fig. 10). There is little change in the thermal conductivity in the basal direction due to variations in either the basal or c spacing of defects. More interestingly, the thermal conductivity in the c-direction varies systematically with the areal density of defects projected on the basal plane. It is insightful to compare this work with Rajabpour and Allaei's study of the effect of interlayer covalent bonding on the thermal conductivity of bilayer graphene [26]; they find that a 2% concentration of sp^3 bonding in an otherwise pristine bilayer of graphene decreases its thermal conductivity by a factor of approximately 60%. They further observe a higher in-plane reduction in κ due to a decrease in high frequency modes. Along the c-direction they observe small changes in low frequency modes. This suggests the significant κ change perpendicular to the basal plane observed in the presence of inter-layer platelets to be mostly due to the additional atoms along this direction while the smaller change in κ along the basal plane could be the result of the introduction of few sp^3 bonds due to the presence of these defects.

Matthiessen's rule states that when more than one source of scattering is present and if the scattering processes that add to the resistivity are independent, then their mobilities can be added as:

$$\frac{1}{\mu} = \frac{1}{\mu_{\text{impurities}}} + \frac{1}{\mu_{\text{lattice}}} + \frac{1}{\mu_{\text{defects}}} + \cdots \tag{7}$$

Based on this premise, and given that $\kappa \propto \mu$, if we consider the additive contributions to the thermal resistance, $r = 1/\kappa$, of the system, it must follow that:

$$r_{\text{defective}} = r_{\text{perfect}} + r_{\text{defects}}, \tag{8}$$

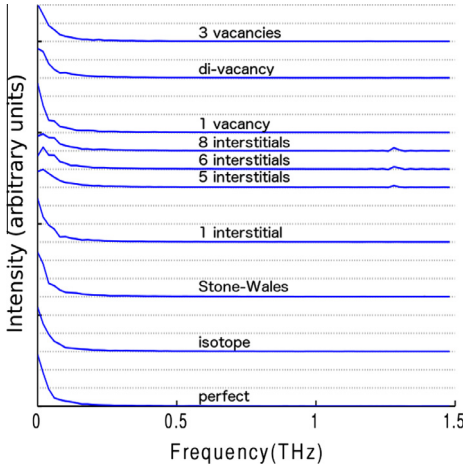

Fig. 9. Discrete cosine transform applied to the c-axis HCACF for different defect types.

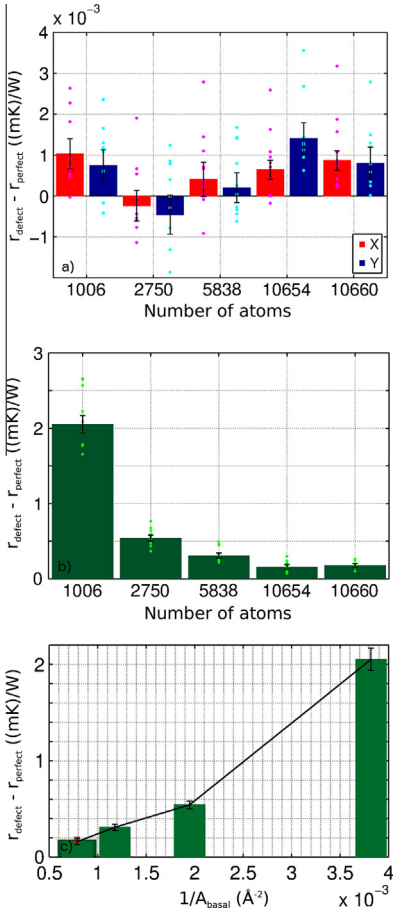

Fig. 10. Hexagonal platelet resistivity (r) and corresponding standard error computed along x and y in the basal plane (a) and along the c-axis (b) for 4 different supercell sizes and for two hexagonal platelets in the same base system. (c) corresponds to a plot of the same resistivities for the hexagonal platelet against the inverse area of the basal plane for each system size. In (c), the value for two-sized platelet is shown in darker green and red errorbar. (For interpretation of the references to colour in this figure legend, the reader is referred to the web version of this article.)

i.e. if the scattering from each defect is independent, we expect the defects to have an additive contribution to the systems' thermal resistance. The additional thermal resistance due to the defect is $r_{\text{defect}} = r_{\text{defective}} - r_{\text{perfect}}$, computed in Fig. 10, where $r_{\text{defective}}$ and r_{perfect} are the thermal resistance of the same size system with and without the defect, respectively. One might therefore expect the thermal resistance for a given system size containing two defects of the same type to be $r_{\text{defective}-2} = r_{\text{perfect}} + 2 \cdot r_{\text{defect}}$, or $r_{\text{defective}-2} = 0.43 \pm 0.06$ W/(mK) for the system with two hexagonal platelets. Instead, the total resistivity value for the two-platelet system is 0.29 ± 0.06 W/(mK) and adding a defect does not double its thermal resistance. The small change in resistivity observed for the two-platelet system compared with the single-platelet system suggests the total defect concentration is not the only determining factor in how clustering defects affect the thermal conductivity in graphite. The linearity observed between the added thermal resistance and the inverse of the basal plane area, A_{basal}, for the different system sizes, as shown in Fig. 10(c), seems to imply that the distribution of defects in the basal plane affects its total resistivity in the c-direction. Size artifacts in the smaller, 1000 atom system and the significantly smaller spacing along z proportional to x and y could contribute to a higher resistivity in this system. It is also relevant that, along the c-axis, for the 6 interstitial platelet $r_{\text{defects}} = 0.16 \pm 0.03$ (mK/W) or four times $6 \cdot r_{\text{defects}} = 0.04 \pm 0.17$ (mK/W) if the single interstitial thermal resistance is used to compute r_{defects}. In other words, the added resistivity contribution of the platelet is greater than the contribution presumed from Matthiessen's rule for the sum of six individual interstitials.

5. Conclusions

In this work we have reported calculations of the reduction in thermal conductivity of graphite due to a series of point defects typical under irradiation. The calculations reveal three important conclusions:

- Clustered interstitial defects are stable (with respect to lone interstitials) and strongly detrimental to the thermal transport particularly along the c-axis direction.
- In addition to lowering the thermal conductivity interstitial platelets also increase the thermal conductivity anisotropy.
- Although the uncertainty in the calculations of κ is large, it is clear that along c the platelets provide an added thermal resistance that is approximately 4 times larger than that of their constituent number of lone interstitials.
- For the system sizes experimented with we observe that the thermal conductivity along the c-direction is sensitive to the spacing of defects in the basal plane.

In pebble bed reactors graphite is used to encapsulate the fissile materials and thus the graphite experiences an extremely large neutron dose. The average fuel temperatures in such a reactor is 1200 K (with peak temperatures expected to stay below 1500 K) [27]. At these temperatures interstitials are highly mobile and readily condense into interstitial platelets. These platelets are responsible for c-axis swelling under irradiation [2]. Our work indicates that this has a doubly negative effect on thermal conductivity; elongating grains along their thermally resistive directions while also increasing the thermal resistance in these directions.

In addition to computing the reduction in thermal conductivity due to defects we have performed a systematic comparison of various numerical strategies for reducing uncertainty in the integration of the HCACF. Our simulations reveal infrequent large heat current fluctuations that are large enough to overwhelm the averaged HCACF. The origin of these fluctuations is unclear to us at this stage and we speculate two possible causes. It is possible that the fluctuations are a manifestation of Fermi–Pasta–Ulam recurrence [28] or some related breakdown of ergodicity over the time period accessible to simulation. An alternative explanation is that the fluctuations are physically realistic processes similar to rogue ocean waves and caused by amplitude dependence of the phonon dispersion in graphite. It has been proposed that carbon nanotubes possess soliton-like heat carriers [29] and it is possible that similar conditions may arise in graphite. These two potential explanations are incompatible and would require one to treat the fluctuations differently: in the first case removing their effect from computed thermal conductivity, and in the latter case performing enough simulations to obtain a statistically significant sampling of these infrequent fluctuations.

Acknowledgments

This work used the Extreme Science and Engineering Discovery Environment (XSEDE), which is supported by National Science Foundation Grant No. OCI-1053575.

References

[1] B.T. Kelly, Prog. Nucl. Energy 2 (4) (1978) 219–269.
[2] B. Kelly, Physics of graphite, in: RES Mechanica Monographs, Kluwer Academic Pub, 1981. <http://books.google.com/books?id=rGR3QgAACAAJ>.

[3] P.K. Schelling, S.R. Phillpot, P. Keblinski, Phys. Rev. B 65 (14) (2002) 144306.
[4] M.S. Green, Marko random processes and the statistical mechanics of time-dependent phenomena. II. Irreversible processes in fluids, J. Chem. Phys. 22 (3) (1954) 398–413, http://dx.doi.org/10.1063/1.1740082. <http://link.aip.org/link/?JCP/22/398/1>.
[5] R. Kubo, J. Phys. Soc. Jpn. 12 (6) (1957) 570–586, http://dx.doi.org/10.1143/JPSJ.12.570. <http://jpsj.ipap.jp/link?JPSJ/12/570/>.
[6] S.G. Volz, G. Chen, Phys. Rev. B 61 (2000) 2651–2656, http://dx.doi.org/10.1103/PhysRevB.61.2651. <http://link.aps.org/doi/10.1103/PhysRevB.61.2651>.
[7] L. Han, M. Budge, P.A. Greaney, Comput. Mater. Sci. 94 (2014) 292–297, http://dx.doi.org/10.1016/j.commatsci.2014.06.008. {IWCMM23} Special Issue, URL http://www.sciencedirect.com/science/article/pii/S0927025614004194.
[8] S. Plimpton, J. Comput. Phys. 117 (1) (1995) 1–19, http://dx.doi.org/10.1006/jcph.1995.1039. <http://www.sciencedirect.com/science/article/pii/S002199918571039X>.
[9] S.J. Stuart, A.B. Tutein, J.A. Harrison, J. Chem. Phys. 112 (14) (2000) 6472–6486.
[10] J. Chen, G. Zhang, B. Li, Phys. Lett. A 374 (23) (2010) 2392–2396.
[11] L.d.S. Oliveira, P.A. Greaney, Mapping thermal resistance around vacancy defects in graphite, MRS Proceedings, vol. 153, Cambridge Univ Press, 2013, pp. 65–70.
[12] D. Sellan, E. Landry, J. Turney, A. McGaughey, C. Amon, Phys. Rev. B 81 (21) (2010) 214305.
[13] J. Che, T. Çağın, W. Deng, W.A. Goddard III, J. Chem. Phys. 113 (16) (2000) 6888–6900.
[14] J. Li, L. Porter, S. Yip, J. Nucl. Mater. 255 (2) (1998) 139–152.
[15] A.J.H. McGaughey, M. Kaviany, Phys. Rev. B 69 (2004) 094303, http://dx.doi.org/10.1103/PhysRevB.69.094303.
[16] D. Morgan, Thermal properties and characteristics of pocofoam, in: Thermal Conductivity 26: Thermal Expansion 14: Joint Conferences, August 6–8, 2001, Cambridge, Massachusetts, USA, DEStech Publications, Inc., 2005, p. 259.
[17] T. Maruyama, M. Harayama, J. Nucl. Mater. 195 (1) (1992) 44–50.
[18] S. Ishiyama, T. Burchell, J. Strizak, M. Eto, J. Nucl. Mater. 230 (1) (1996) 1–7.
[19] K. Niwase, Phys. Rev. B 52 (22) (1995) 15785.
[20] E. Bitzek, P. Koskinen, F. Gähler, M. Moseler, P. Gumbsch, Phys. Rev. Lett. 97 (17) (2006) 170201.
[21] L. Li, S. Reich, J. Robertson, Phys. Rev. B 72 (18) (2005) 184109.
[22] R.H. Telling, C.P. Ewels, A. Ahlam, M.I. Heggie, Nat. Mater. 2 (5) (2003) 333–337.
[23] K. Nordlund, J. Keinonen, T. Mattila, Phys. Rev. Lett. 77 (4) (1996) 699.
[24] Y. Miyamoto, A. Rubio, S. Berber, M. Yoon, D. Tománek, Phys. Rev. B 69 (12) (2004) 121413.
[25] E. Kaxiras, K. Pandey, Phys. Rev. Lett. 61 (23) (1988) 2693.
[26] A. Rajabpour, S. Vaez Allaei, Appl. Phys. Lett. 101 (5) (2012). pp. 053115–053115.
[27] S. Ion, D. Nicholls, R. Matzie, D. Matzner, Pebble bed modular reactor the first generation iv reactor to be constructed, in: World Nuclear Association Annual Symposium, 2003, pp. 3–5.
[28] E. Fermi, J. Pasta, S. Ulam, Studies of nonlinear problems, Los Alamos Report LA-1940, 1955, p. 978
[29] C. Chang, D. Okawa, H. Garcia, A. Majumdar, A. Zettl, Nanotube phonon waveguide, Phys. Rev. Lett. 99 (4) (2007) 045901.